Optics Letters

Development of yellow-light TiO_2 integrated photonics

Zequn Chen,[1,2] Yiheng Tang,[1,2] Maoliang Wei,[3,4] Xiaojing Li,[4,5] Boshu Sun,[1,2] Yingchun Wu,[1,2] Sishuo Zou,[3,4] Ji Huang,[1,2] Ke Si,[4,6] Wei Gong,[4,5] Hongtao Lin,[3,4] and Lan Li[1,2,7,*]

[1]Institute of Advanced Technology, Westlake Institute for Advanced Study, Hangzhou 310024, China
[2]Zhejiang Key Laboratory of 3D Micro/Nano Fabrication and Characterization, School of Engineering, Westlake University, Hangzhou 310030, China
[3]The State Key Lab of Brain-Machine Intelligence, College of Information Science and Electronic Engineering, Zhejiang University, Hangzhou 310027, China
[4]MOE Frontier Science Center for Brain Science & Brain-Machine Integration, Zhejiang University, Hangzhou 310027, China
[5]Nanhu Brain-Computer Interface Institute, Hangzhou 311100, China
[6]College of Optical Science and Engineering, Zhejiang University, Hangzhou 310027, China
[7]Westlake Institute for Optoelectronics, Fuyang, Hangzhou, Zhejiang 311421, China
*lilan@westlake.edu.cn

Received 27 February 2025; revised 15 April 2025; accepted 22 April 2025; posted 22 April 2025; published 16 May 2025

Visible-light photonic integrated circuits (PICs) are rapidly emerging as a crucial technology to overcome the scaling challenges in quantum information processing and biosensing. Titanium dioxide (TiO_2), with its high transparency in the visible range, is regarded as a promising material for facilitating the development of high-performance visible-light integrated systems. In this paper, we introduce a series of passive TiO_2 integrated devices, which include waveguides, multimode interferometers (MMIs), and thermo-optic switches (TOSs), monolithically integrated for the first time to our knowledge at a working wavelength of 589 nm. A propagation loss of 5.46 ± 0.17 dB/cm demonstrates a significant improvement over previous reports on yellow-light TiO_2 waveguides. This study marks the first fabrication of a TOS operating at 589 nm, featuring a TiO_2 core and polymer cladding. Notably, it achieves a power consumption (P_π) of 8.24 mW, which represents a threefold reduction compared to silicon nitride-based TOSs operating in the visible spectrum. These results offer new insight into the design and fabrication of visible waveguide-integrated devices, paving the way for future emerging applications, such as quantum information, sensors, and biomedical science.

https://doi.org/10.1364/OL.560919

Silicon photonics utilizes microelectronics manufacturing technologies, enabling the large-scale production of dense and complex photonic integrated circuits (PICs) in foundries. Extending silicon photonics to the visible spectrum opens up new opportunities for emerging applications. Visible-light integrated photonics represents a promising frontier, encompassing a diverse array of applications, including quantum information processing [1–3], nonlinear optics [4], underwater communication [5], scanning displays [6,7], optical sensors [8], flow cytometry [9], and optogenetics [10–15].

In visible-wavelength silicon photonics, optical waveguides are commonly constructed using silicon nitride (SiN, 1.2 dB/cm at 488 nm [16]) or aluminum oxide (Al_2O_3, 0.8 dB/cm at 450 nm [17]) layers with silicon dioxide (SiO_2) cladding, built on silicon or silicon-on-insulator (SOI) substrates. Currently, visible-light photonic platforms based on SiN [2,11], [18–21] or Al_2O_3 [22] materials have been successfully developed on 100 mm, 200 mm, and 300 mm diameter silicon wafers. These platforms integrate various components, including waveguides, gratings, power splitters, interferometers, and detectors. Furthermore, large-scale integrated chip-level systems operating in the visible spectrum demand micron-scale phase modulators with low-power consumption or low driving voltage. Meeting these requirements presents significant challenges for visible-light integrated photonics. While materials such as SiN [10], aluminum nitride (AlN) [23], and SiO_2 [24] are compatible with complementary metal–oxide–semiconductor (CMOS) fabrication processes, they exhibit inherently weak thermo-optic (TO) and electro-optic (EO) effects. For instance, the TO coefficient (TOC) of SiN is significantly smaller than that of silicon. In the visible-wavelength range, TO phase modulators utilizing SiN waveguides typically require device lengths on the order of hundreds of micrometers and power consumption in the tens of milliwatts to achieve π-phase modulation [6,10]. Lithium niobate (LN) [25–27], as a novel material platform for integrated photonics, offers ultra-low propagation loss, though it is not compatible with CMOS. Given its large EO coefficient (EOC), state-of-the-art visible-light LN waveguide phase modulators require a half-wave voltage-length product ($V_\pi L$) of 1.6 V·cm, which means the device length driven by CMOS-level voltages is approximately 1 cm [26]. Liquid crystal cladding provides a modulation mechanism with a smaller $V_\pi L$, but it is inherently

limited in supporting high-speed modulation [28]. In recent years, TO modulators and switches integrated with polymer waveguides have achieved low-power operation due to the larger TOC of the polymer. However, the relatively low refractive index of the polymers necessitates larger device dimensions, typically on the scale of tens of millimeters, which poses challenges for miniaturization [29].

Titanium dioxide (TiO_2), as an emerging integrated photonic material, has garnered much attention in recent years. TiO_2 exhibits a wideband transparency ranging from visible to the near-infrared wavelengths (0.4–10 μm), along with biocompatibility [30], nonlinearity [31,32], and a higher refractive index [30] and TOC (-0.5 to $-2.4\times10^{-4}\,K^{-1}$) [33] compared to AlN and SiN. Additionally, it is compatible with CMOS processes and can be fabricated at near-room-temperature conditions [34], enabling more compact integration. These attributes have positioned TiO_2 as a promising material for applications in sensing devices [35], thermal insulation devices [36,37], and PICs [38,39]. Furthermore, the integration of TiO_2 with polymers, leveraging their mutually negative TOCs, has demonstrated a synergistic effect, facilitating the development of highly efficient thermo-optic switches (TOSs) [34] and modulators [38] operating within the telecommunication wavelength range. However, research on TiO_2-based devices in the visible-wavelength range remains scarce. Existing studies indicate that propagation loss in TiO_2-based waveguides at visible wavelengths remains relatively high [40–42], underscoring a critical area for further exploration and optimization.

In this work, we demonstrate a yellow-light TiO_2 platform integrated with passive components, including waveguides, 1×2 multimode interferometers (MMIs), 2×2 MMIs, and yellow-light TOSs (VTOSs) based on Mach–Zehnder interferometer MMIs (MZI-MMIs). These components feature a TiO_2 waveguide core and polymer cladding. The propagation loss of the waveguide at a working wavelength of 589 nm is measured to be 5.46 ± 0.17 dB/cm. The insertion loss of the 1×2 MMIs and 2×2 MMIs are 3.34 ± 0.04 dB and 3.29 ± 0.21 dB, respectively, meeting the low insertion loss requirements for VTOSs. Leveraging the negative TOCs of both the polymer substrate and TiO_2, the π phase-shift power consumption (P_π) of the TiO_2 VTOS is 8.24 mW, which is lower than that of certain SiN-based VTOSs. The VTOS exhibits rise and fall times of 68.2 μs and 57.4 μs, respectively. Additionally, the higher refractive index of TiO_2 enables the VTOS to achieve a footprint two orders of magnitude smaller than polymer-based VTOS. This approach demonstrates the potential for large-scale, monolithic integration of photonic devices at visible wavelengths.

A schematic of the yellow-light device preparation process is shown in Fig. 1. Firstly, a 3 μm layer of colorless polyimide (CPI), a 30 nm layer of alumina (Al_2O_3), and a 120 nm sputtered TiO_2 thin film were sequentially deposited on the Si/SiO_2 substrates. Secondly, the TiO_2 waveguide-integrated device patterns were defined using electron-beam lithography and inductively coupled plasma reactive ion etching, followed by 500 nm SU-8 coating on the TiO_2 device with 105°C baking for 1 min and 175°C baking for 5 min, obtaining the passive device. For VTOS fabrication, heater electrodes consisting of 100 nm Ti/5 nm Au and contact pads comprising 5 nm Ti/100 nm Au were sequentially deposited onto the pre-fabricated devices. Thirdly, a second 2.5 μm SU-8 layer was applied, followed by the photolithographic patterning to open the pad window for probe contact and the same annealing process as mentioned above.

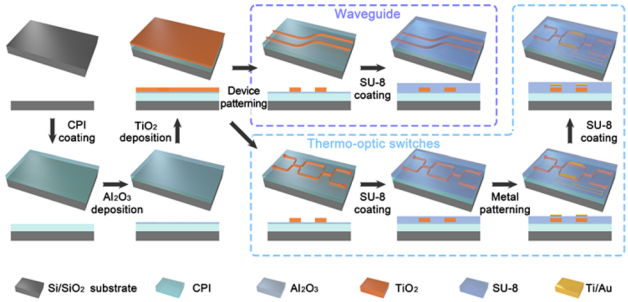

Fig. 1. Diagram of the fabrication process for TiO_2 waveguide-integrated devices operating at visible wavelengths.

The refractive index of CPI, SU-8, and TiO_2 at a wavelength of 589 nm is 1.72, 1.60, and 2.43, respectively. For the characterization of the passive devices, the device was coupled to input and output fibers (3 μm, OZ Optics) using grating couplers inclined at 10° to enhance coupling efficiency. A supercontinuum laser system (SC-PRO-ADTF) was employed as the light source, and the optical transmission spectrum was recorded using a spectrometer (ANDO AQ6315A). For testing the VTOSs, a semiconductor laser (MXL-W-589) served as the light source, while a sourcemeter (Keithley 2450) supplied the voltage to heat the waveguide. The emitted optical signal was measured with a powermeter. An arbitrary waveform generator (AWG, UGT932) provided the modulation voltage for dynamic characterization. The optical output was connected to a photodetector (Thorlabs PDA015A), and an oscilloscope (Siglent SDS5104X) captured the modulation signals to evaluate the device's response time.

We first characterized the propagation loss of the TiO_2 waveguide at a wavelength of 589 nm. Figure 2(a) shows a top-view image of the waveguide propagating light. The single-mode condition of the TiO_2 waveguide at 589 nm is achieved with a height of 100 nm and a width of 370 nm (the inset of Fig. 2(a)). To further minimize the propagation loss, the width of the straight waveguide was increased to 1 μm, while the curved sections employed single-mode waveguides with Euler geometric bends to reduce bending loss. A 30 μm adiabatic tapered waveguide was used to seamlessly connect the straight and curved sections. Using the cut-back method, the propagation loss at 589 nm was measured to be 5.46 ± 0.17 dB/cm, which represents a significant improvement compared to the previously reported visible-light TiO_2 waveguides (Table S1 in Supplement 1, Section 1). The detailed discussions of the propagation loss are described in Supplement 1, Section 1. As demonstrated in our previous work [38], waveguide roughness results in a propagation loss of approximately 1 dB at 1310 nm. This loss is expected to increase in the visible spectrum due to the enhanced interaction of shorter wavelengths with the waveguide sidewalls [16]. To further minimize propagation loss, optimization of the etching process is essential, which can be achieved by replacing the fluorine-based atmosphere with a halogen-based atmosphere, such as Cl_2 and BCl_3 [32]. Additionally, improvements in the patterning process, such as substituting the photoresist mask with a hard mask, such as chromium (Cr) [31], could significantly enhance waveguide performance.

As indispensable components in cascading integrated photonic devices, the yellow-light TiO_2 1×2 and 2×2 MMI were fabricated and characterized. The cascade of 1×2 and 2×2 MMI devices are shown in Figs. 3(a) and 3(c), respectively. The

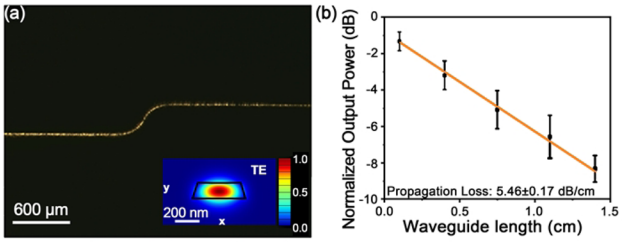

Fig. 2. (a) Top-view optical image of the waveguide propagating light at 589 nm. The inset is the simulated electric field magnitude $|E|$ shown for the TE polarization of the waveguide at 589 nm. (b) Measured transmission of waveguides as a function of the length of waveguides at 589 nm.

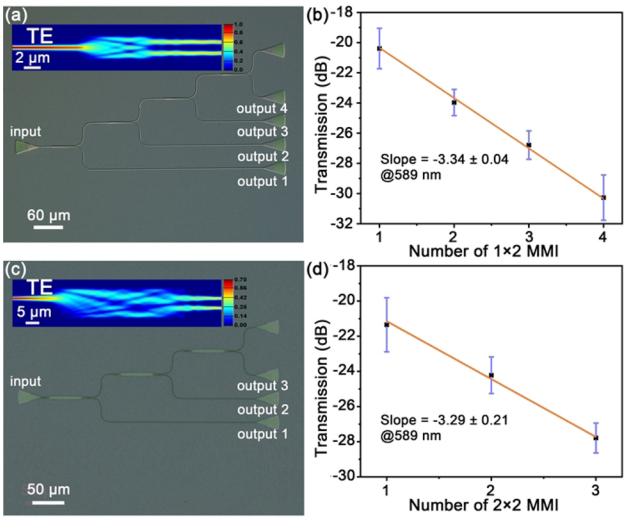

Fig. 3. (a) and (c) Microscope images of the yellow-light TiO_2 waveguide device based on a cascade of 1×2 and 2×2 MMIs, respectively. The inserts are the simulated electric field distributions of the optimized yellow-light TiO_2 1×2 and 2×2 MMI, respectively. (b) and (d) Measured transmission of cascaded TiO_2 1×2 and 2×2 MMI trees as a function of number of 1×2 and 2×2 MMI, respectively.

length and width of the design-optimized TiO_2 1×2 MMI region are 10.5 μm and 2.4 μm, respectively, with a waveguide width of 0.37 μm. For the 2×2 MMI region, the length and width are 53.4 μm and 4.8 μm, respectively, with the same waveguide width of 0.37 μm. The insets of Figs. 3(a) and 3(c) display the simulated electric field distribution of the mode profiles for the optimized 1×2 and 2×2 MMI, demonstrating low cross talk at the input and uniform power splitting at the output. As depicted in Figs. 3(b) and 3(d), the measured insertion loss of TiO_2 1×2 and 2×2 MMI are approximately -3.34 ± 0.04 dB and -3.29 ± 0.21 dB per MMI, respectively, measured from inputs to outputs.

The TOS is another crucial component in cascade-integrated photonic systems. Following the verification of waveguide propagation loss and optical splitter's performance, a TiO_2 TOS for yellow-light routing was fabricated for the first time. The process began with finite element modeling (FEM) analysis to simulate VTOS devices. Figure 4(a) illustrates the fundamental TE mode of the TiO_2 waveguide cross section featuring a width of 370 nm, a height of 100 nm, and a sidewall angle of 67°.

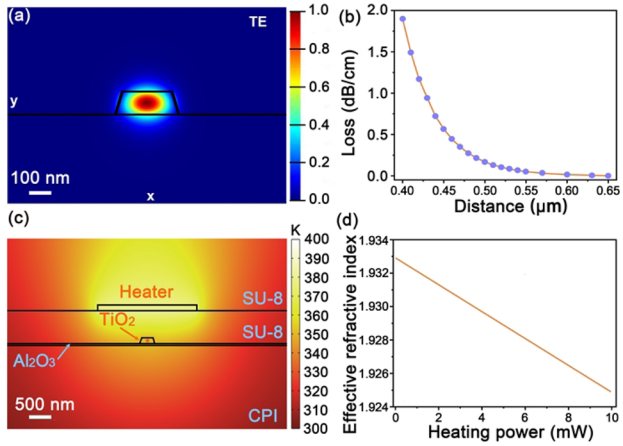

Fig. 4. (a) Fundamental electric field magnitude $|E|$ shown for the TE polarization of the sputtered TiO_2 waveguide at 589 nm. (b) Simulated propagation loss of the waveguide as a function of the verticle distance between the heater electrode and the TiO_2 waveguide. (c) Calculated temperature distribution at a simulated heating power of P_π (7.5 mW). (d) Simulated effective refractive index of the TiO_2 waveguide versus heating power.

These waveguides exhibit strong field confinement, ensuring high dispersion and exceptional sensitivity to minor variations in material refractive index while maintaining low bending loss. These attributes are instrumental in designing scalable, reconfigurable, and miniaturized multifunctional devices. Considering the simplicity and cost-effectiveness of the fabrication process, Ti was chosen as the heater material, with a thickness of 100 nm, a width of 5 μm, and a length of 60 μm. Moreover, a verticle space of 0.6 μm was introduced between the heater and the waveguide to optimize the balance between waveguide propagation loss and heating efficiency. Figure 4(c) illustrates the temperature distribution of the waveguide under a heating power of 7.5 mW. The temperature at the center of the waveguide, indicated by the red point in Fig. 4(c), is approximately 357 K. The detailed discussions of the SU-8 stability are described in Supplement 1, Section 2. Figure 4(d) shows the relationship between the effective refractive index of the TiO_2 waveguide and the applied heating power. The phase tuning $\Delta\varphi$ of the waveguide can be expressed as follows [34]:

$$\Delta\varphi = \frac{2\pi L}{\lambda_0}\left(\frac{dn}{dT}\right)\Delta T, \tag{1}$$

where λ_0 is the working wavelength, L is the heater length, dn/dT represents the TOC of TiO_2, and ΔT is the change of temperature. The theoretically calculated P_π of the VTOS is 7.5 mW. Compared to TOSs operating at 1310 nm, the shorter wavelength of visible light allows for a smaller distance between the heating electrode and the waveguide. This reduced distance shortens the heat conduction path, thereby lowering the power consumption required to achieve a π phase shift.

Furthermore, we characterized the VTOS based on the Mach–Zehnder interferometer (MZI)-MMI structures. Figure 5(a) shows the normalized transmission of the bar and cross ports at 589 nm under varying heating power applied to one arm. The VTOS exhibits a cross talk of −17.7 dB, an extinction ratio (ER) of 17.9 dB, and an insertion loss of ~0.6 dB. At a bias voltage of 1.76 V, the device achieves π phase shift

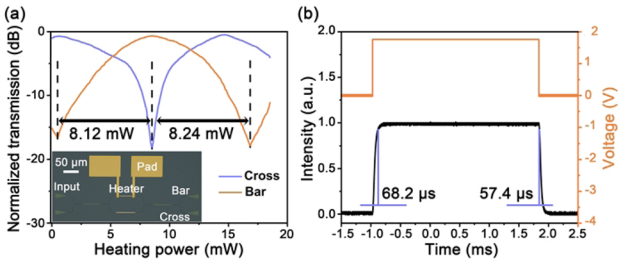

Fig. 5. (a) Normalized transmission of the cross and bar ports of the TiO_2 VTOS at 589 nm under different applied heating power. The inset is the top-view image of the device. (b) Time response of the MZI-MMI-based TiO_2 VTOS.

with a power consumption of 8.24 mW. The dynamic response demonstrated rise/fall times of 68.2 μs and 57.4 μs, respectively, as shown in Fig. 5(b). These performance metrics make the device suitable for applications in fields such as optogenetics [13] and PICs [9,43]. Meanwhile, the P_π of 8.24 mW is significantly lower than that of some visible-light SiN-based TOSs (Table S2 in Supplement 1, Section 2), highlighting the superior TOC of TiO_2 and the synergistic effect between TiO_2 and polymer substrates with negative TOC [34,38]. Additionally, the device footprint is two orders of magnitude smaller than that of visible-light polymer-based TOSs (Table S2 in Supplement 1, Section 2), demonstrating the advantages of the high-index-contrast platform. This compact design offers promising benefits for wearable and implantable devices by reducing system size and minimizing potential damage to biological tissues [12].

In conclusion, we have successfully prepared yellow-light TiO_2 integrated passive components using a monolithic integration approach, achieving significant performance improvements. The propagation loss was reduced to 5.46 ± 0.17 dB/cm, while the insertion loss was 3.34 ± 0.04 dB for the 1×2 MMI and 3.29 ± 0.21 dB for the 2×2 MMI. Additionally, the VTOSs demonstrated a low P_π value of 8.24 mW. Given that TiO_2 can be deposited under near-room-temperature conditions, this technology shows great potential for applications in three-dimensional stacked photonic integration [44]. We envisage that this fabrication approach for visible-light waveguide integration will substantially advance and broaden the development and application of integrated photonic devices operating in the visible spectrum.

Funding. Key Research and Development Program of Zhejiang Province (2024C03150, 2024SSYS0019, 2024SSYS0031, 2021C03001); National Natural Science Foundation of China (62175202); STI 2030—Major Projects (2021ZD0200401); Key Project of Westlake Institute for Optoelectronics (2023GD003/110500Y0022303); MOE Frontier Science Center for Brain Science & Brain-Machine Integration, Zhejiang University; Leading Innovative and Entrepreneur Team Introduction Program of Zhejiang (2020R01005, 202099144).

Acknowledgment. The authors would like to acknowledge the Westlake Center for Micro/Nano Fabrication at Westlake University and ZJU Micro-Nano Fabrication Center at Zhejiang University for the facility support.

Disclosures. The authors declare no conflicts of interest.

Data availability. Data underlying the results presented in this paper are not publicly available at this time but may be obtained from the authors upon reasonable request.

Supplemental document. See Supplement 1 for supporting content.

REFERENCES

1. K. K. Mehta, C. Zhang, M. Malinowski, *et al.*, Nature **586**, 533 (2020).
2. M. Dong, G. Clark, A. J. Leenheer, *et al.*, Nat. Photonics **16**, 59 (2022).
3. R. J. Niffenegger, J. Stuart, C. Sorace-Agaskar, *et al.*, Nature **586**, 538 (2020).
4. D. J. Moss, R. Morandotti, A. L. Gaeta, *et al.*, Nat. Photonics **7**, 597 (2013).
5. Z.-Q. Yan, C.-Q. Hu, Z.-M. Li, *et al.*, Photonics Res. **9**, 2360 (2021).
6. M. Chul Shin, A. Mohanty, K. Watson, *et al.*, Opt. Lett. **45**, 1934 (2020).
7. M. Raval, A. Yaacobi, and M. R. Watts, Opt. Lett. **43**, 3678 (2018).
8. C. Gong, X. Yang, S.-J. Tang, *et al.*, Light: Sci. Appl. **12**, 292 (2023).
9. D. Geuzebroek, R. Dekker, E. Klein, *et al.*, Sens. Actuators, B **223**, 952 (2016).
10. A. Mohanty, Q. Li, M. A. Tadayon, *et al.*, Nat. Biomed. Eng. **4**, 223 (2020).
11. W. D. Sacher, X. Luo, Y. Yang, *et al.*, Opt. Express **27**, 37400 (2019).
12. Z. Chen, X. Li, Y. Tang, *et al.*, Cell Rep. Phys. Sci. **5**, 102217 (2024).
13. L. C. Moreaux, D. Yatsenko, W. D. Sacher, *et al.*, Neuron **108**, 66 (2020).
14. K. Jung, S. Krüssel, S. Yoo, *et al.*, Nat. Neurosci. **27**, 2178 (2024).
15. N. Utashiro, D. A. A. MacLaren, Y.-C. Liu, *et al.*, Nat. Commun. **15**, 5772 (2024).
16. M. Corato-Zanarella, X. Ji, A. Mohanty, *et al.*, Opt. Express **32**, 5718 (2024).
17. E. McKay, N. G. Pruiti, S. May, *et al.*, Sci. Rep. **13**, 19917 (2023).
18. Y. Lin, Z. Yong, X. Luo, *et al.*, Nat. Commun. **13**, 6362 (2022).
19. A. T. Mashayekh, T. Klos, D. Geuzebroek, *et al.*, Opt. Express **29**, 8635 (2021).
20. T. Xue, A. Stalmashonak, F.-D. Chen, *et al.*, Sci. Rep. **14**, 13812 (2024).
21. T. J. Morin, L. Chang, W. Jin, *et al.*, Optica **8**, 755 (2021).
22. G. N. West, W. Loh, D. Kharas, *et al.*, APL Photonics **4**, 026101 (2019).
23. T.-J. Lu, M. Fanto, H. Choi, *et al.*, Opt. Express **26**, 11147 (2018).
24. S. H. Lee, D. Y. Oh, Q.-F. Yang, *et al.*, Nat. Commun. **8**, 1295 (2017).
25. M. Zhang, C. Wang, R. Cheng, *et al.*, Optica **4**, 1536 (2017).
26. B. Desiatov, A. Shams-Ansari, M. Zhang, *et al.*, Optica **6**, 380 (2019).
27. D. Renaud, D. R. Assumpcao, G. Joe, *et al.*, Nat. Commun. **14**, 1496 (2023).
28. M. Notaros, A. G. Coleto, M. Raval, *et al.*, Opt. Lett. **49**, 1041 (2024).
29. B. Lin, X. Wang, J. Lv, *et al.*, Opt. Lett. **45**, 4448 (2020).
30. L. Li, P. Zhang, W.-M. Wang, *et al.*, Sci. Rep. **5**, 13832 (2015).
31. M. Fu, Y. Zheng, G. Li, *et al.*, Photonics Res. **9**, 1416 (2021).
32. M. Fu, Y. Zheng, G. Li, *et al.*, Opt. Express **28**, 39084 (2020).
33. H. Park, J. Jung, Y. Zhang, *et al.*, ACS Appl. Electron. Mater. **4**, 651 (2022).
34. Z. Chen, M. Wei, B. Sun, *et al.*, Opt. Lett. **48**, 3239 (2023).
35. X. Zhao, B. Fan, A. Veeraraghavan, *et al.*, in *2022 Conference on Lasers and Electro-Optics (CLEO)* (2022), pp. 1–2.
36. F. Qiu, A. M. Spring, and S. Yokoyama, ACS Photonics **2**, 405 (2015).
37. B. Guha, J. Cardenas, and M. Lipson, Opt. Express **21**, 26557 (2013).
38. Z. Chen, M. Wei, Y. Luo, *et al.*, Opt. Mater. Express **12**, 4061 (2022).
39. H. Yu and F. Qiu, Opt. Lett. **47**, 2093 (2022).
40. I. Hegeman, M. Dijkstra, F. B. Segerink, *et al.*, Opt. Express **28**, 5982 (2020).
41. M. Furuhashi, M. Fujiwara, T. Ohshiro, *et al.*, AIP Adv. **1**, 032102 (2011).
42. C. C. Evans, C. Liu, and J. Suntivich, Opt. Express **23**, 11160 (2015).
43. Y. Su, Y. He, X. Guo, *et al.*, ACS Photonics **10**, 2020 (2023).
44. J. Yue, X. Sun, C. Wang, *et al.*, Opt. Express **31**, 19415 (2023).